JOURNAL OF THERMOPHYSICS AND HEAT TRANSFER
Vol. 24, No. 1, January–March 2010

Unstructured Cartesian Grid Methodology for Inviscid Nonequilibrium Hypersonic Flows

Jinwook Lee,* Alessio Orsini,† and Stephen M. Ruffin‡
Georgia Institute of Technology, Atlanta, Georgia 30332

DOI: 10.2514/1.40257

In this work, a solution-adaptive unstructured Cartesian grid solver for thermochemical nonequilibrium hypersonic flows with a two-temperature model is developed. The Cartesian grid methodology offers the convenience of automatic grid generation over three-dimensional complex geometries with minimum user intervention. At the same time, an accurate higher-order flux calculation over unstructured-grid topologies is provided. To avoid convergence problems in the explicit flow solver, a point-implicit method is adopted to discretize the source terms. The AUSMPW+ numerical scheme with MUSCL data reconstruction is used, preventing nonphysical oscillations and carbuncle phenomena. The accuracy of the present methodology was verified against DPLR (NASA Ames Research Center's structured-grid nonequilibrium flow solver), showing a good agreement between the two codes. As expected, the AUSMPW+ scheme effectively resolved the large gradients of the flow properties at the shock waves. In parallel, the point-implicit technique used for the source terms allows the original Courant–Friedrichs–Lewy constraints of the explicit solver to be maintained.

Nomenclature

A_{ij}	=	slope coefficient for vibrational relaxation
B_r, C_r, D_r	=	Arrenius coefficients
$\bar{c}_j$	=	species average molecular velocity
c_v	=	specific heat at constant volume
E_t	=	total energy per unit volume
E_{ve}	=	vibrational–electronic energy per unit volume
e_i	=	species internal energy per unit volume
$\mathbf{F}$, $\mathbf{G}$, $\mathbf{H}$	=	flux vectors
$\hat{g}$	=	molar Gibbs free energy
h_0	=	heat of formation per unit mass
$\mathbf{I}$	=	identity matrix
K_c	=	equilibrium constant
k	=	Boltzmann constant
k_b	=	backward-reaction-rate coefficient
k_f	=	forward-reaction-rate coefficient
N_r	=	number of chemical reactions
N_s	=	number of chemical species
N_{sp}	=	number of polyatomic chemical species
n_j	=	species number density
M	=	Mach number
MW	=	molecular weight
p	=	pressure
$\mathbf{q}$	=	vector of species partial densities
$\mathbf{R}$	=	vector of species fluxes integrated over a cell surface
$\mathcal{R}$	=	universal gas constant
$\mathbf{S}$	=	source terms vector
s	=	Park's exponent
T	=	translational–rotational temperature
T_d	=	dissociation temperature for reaction rates
T_{ve}	=	vibrational–electronic temperature
t	=	time
$\mathbf{U}$	=	state vector
u, v, w	=	velocity components
V	=	cell volume
$\mathbf{v}$	=	velocity vector
x, y, z	=	Cartesian coordinates
x_i	=	species molar fractions
y_i	=	species mass fractions
α	=	numerical diffusivity control constant for AUSMPW+
α_c	=	grid coarsening and refining parameter
θ_j	=	characteristic vibrational temperatures
$\tilde{\kappa}$	=	mixture-specific constant for radiation
$\mu_{i,j}$	=	reduced mass of the species i and j
ν'	=	stoichiometric coefficient for reactants
ν''_i	=	stoichiometric coefficient for products
ρ	=	density
σ_c	=	root mean square of adaption parameters
σ_j	=	species effective cross section
τ_c	=	composition gradient-based grid adaption parameter
τ_i	=	species vibrational relaxation time
τ^{MW}	=	molar-averaged vibrational relaxation time
τ^P	=	vibrational relaxation time of Park's correction
ω_i	=	species source terms
ω_{ve}	=	vibrational–electronic energy source term

Subscripts

i, j, k	=	chemical species index
n	=	time-step index
r	=	chemical reactions index
rot	=	rotational energy mode
shock	=	shock wave
tr	=	translational energy mode
ve	=	vibrational–electronic energy mode

Presented as Paper 4548 at the AIAA Thermophysics Conference, Miami, FL, 25–28 June 2007; received 5 August 2008; revision received 16 July 2009; accepted for publication 20 July 2009.

*Graduate Research Assistant, School of Aerospace Engineering; currently Member of the Technical Staff, The Aerospace Corporation.

†Graduate Student, School of Aerospace Engineering; currently Aero-Engine Performance Engineer, AVIO Aerospace Propulsion.

‡Associate Professor, School of Aerospace Engineering. Senior Member AIAA.

I. Introduction

IN THE past years, the increasing interest in various types of vehicles operating in the hypersonic regime has stimulated the development of numerous nonequilibrium flow solvers. To investigate the optimum configuration for various types of hypersonic vehicles, a nonequilibrium computational fluid dynamics tool with advanced grid techniques, which can handle complex geometries with

minimum user intervention, is desired. To fulfill these requirements, several adaptive unstructured-grid solvers have been developed.

Aftosmis and Baron [1] developed a 2-D solution-adaptive algorithm to resolve shock waves in hypersonic chemical nonequilibrium flows. Such a method locally refines the computational cells by subdividing the existing curvilinear mesh with a criterion based on density gradients. This adaptive technique saves a considerable amount of computational time compared with globally refined structured grids and reduces the human intervention. However, this method requires an initial effort to generate the curvilinear grids and is not adequate for complex geometries.

Gnoffo [2] and Gnoffo and White [3] reengineered and synthesized the existing analysis capabilities in LAURA (structured-grid hypersonic Navier–Stokes solver focused on external flow) and VULCAN (structured-grid Navier–Stokes solver focused on internal flows) into the well-known tetrahedral grid based unstructured-grid solver, FUN3D. The aim of this synthesis was to significantly reduce the time and effort in generating grids and to obtain more control over the grid quality around complex shapes by using advanced grid topologies. However, the stagnation-point heat flux was poorly predicted by FUN3D when compared with the results of LAURA. According to their analyses, the primary cause of this accuracy degradation arises from how the inviscid terms are processed across the shock wave and shock layer to the edge of the boundary layer; not from a poor formulation of viscous terms across the boundary layer itself. Other studies [4,5] also identified the difficulties with obtaining second-order-accurate flux reconstruction on stretched tetrahedral cells.

With the preceding issues in mind, Nompelis et al. [5,6] developed a new implicit unstructured-grid solver. They were able to improve the solution quality by using hexahedral and prismatic structured grids whenever possible, and tetrahedral grid elements only when necessary, with the cost of increased user intervention. However, whereas the high-quality hexahedral grid near the surface produced a good solution accuracy, the tetrahedral grid near the bow shock introduced numerical errors. This work demonstrated the basic principle that a good grid design is still critical for accurate solutions even in a modern unstructured-grid solver.

The objective of this research is to provide an existing flow solver, NASCART-GT, with the capability to handle 3-D thermochemical nonequilibrium inviscid flows. NASCART-GT is a solution-adaptive unstructured Cartesian-grid-based solver for calorically perfect gases. Cartesian grids offer some advantages in calculating higher-order inviscid fluxes over other grid topologies such as tetrahedral or prismatic grids. A Cartesian grid uses perfectly orthogonal cells with the solid body cutting a background computational mesh. It does not require complex coordinate transformations or computation of contravariant velocities such that the truncation error is significantly reduced. Also, the Cartesian-grid-based approach has the advantage of a relative computational simplicity due to the elimination of a body-fitted mesh. Its ability to automatically generate grids over very complex geometries by intersecting the solid surfaces provides advantages when using irregularly deforming geometries. The governing equations already implemented in NASCART-GT are Euler, Euler with integral boundary-layer method, and Navier–Stokes with a two-equation (K-ε) turbulence model. Roe's averaging and AUSMPW+ scheme with MUSCL data reconstruction are available for inviscid fluxes; however, the latter performs better in the hypersonic flow regime. The grid adaption criteria used are velocity divergence, vorticity, and gradient of K-ε.

For this analysis, the capability to handle thermochemical nonequilibrium inviscid flows is added to the solver to simulate high-temperature-gas effects; a grid adaption method based on chemical species gradients is implemented to increase the accuracy and stability of the solution. Although Cartesian grids have attractive features in computing inviscid fluxes compared with other grid topologies, only one previous work in this area was done (Tu [7] in 2001). In his work, Tu developed a solution-adaptive Cartesian-grid-based thermochemical nonequilibrium solver for 2-D flows in a platform completely different from NASCART-GT.

Application and demonstration of thermochemical nonequilibrium analysis to 3-D solution-adaptive Cartesian grid computational fluid dynamics formulation has not been done before the present work. This work seeks to incorporate successfully used two-temperature thermochemical nonequilibrium chemistry models. Solution adaption to chemical species gradients is found to be needed for numerical stability as well as accuracy. A successful methodology for doing so is presented in this paper.

The accuracy of the thermochemical development work is verified against DPLR (NASA Ames Research Center's structured-grid nonequilibrium solver). It should be noted that this paper does not seek to compare computational efficiency of these two codes or their methodologies. Both codes are parallelized, but there is overhead due to the unstructured-grid nature of the adaptive Cartesian approach so that it takes more CPU time per grid point per iteration compared with the structured-grid methodology. In addition, for many geometries, the number of grid points (and thus CPU time) for a structured-grid methodology is smaller than that for a Cartesian-grid-based approach. The prime benefit of the Cartesian methodology, however, lies in its ability to model complex geometries, multiple bodies in the flow, cavities, and protrusions that cause difficulties in grid generation for structured-grid solvers. The automated grid generation and grid adaptation capabilities of the Cartesian approach are particularly attractive for complex bodies. The focus of this paper is not efficiency or complex body treatment, however, it is rather in the ability to accurately represent thermochemical nonequilibrium physics in an adaptive Cartesian framework with a fidelity similar to the well-validated DPLR code.

In general, the results of the improved NASCART-GT agree well with the reference code, as demonstrated from two of the three test cases presented: a hypersonic circular cylinder in air mixture and the Huygens probe entering the Titan atmosphere.

II. Governing Equations

The conservative form of the mass, momentum, total energy, species, and vibrational–electronic energy equations governing an inviscid thermochemical nonequilibrium flow in Cartesian coordinates is

$$\frac{\partial \mathbf{U}}{\partial t} + \frac{\partial \mathbf{F}}{\partial x} + \frac{\partial \mathbf{G}}{\partial y} + \frac{\partial \mathbf{H}}{\partial z} = \mathbf{S} \tag{1}$$

The state vector $\mathbf{U}$; the fluxes vectors $\mathbf{F}$, $\mathbf{G}$, and $\mathbf{H}$; and the source terms vector $\mathbf{S}$ read

$$\mathbf{U} = \begin{pmatrix} \rho \\ \rho u \\ \rho v \\ \rho w \\ E_t \\ \rho_1 \\ \vdots \\ \rho_{N_s} \\ E_{\text{ve}} \end{pmatrix}, \quad \mathbf{F} = \begin{pmatrix} \rho u \\ \rho u^2 + p \\ \rho uv \\ \rho uw \\ u(E_t + p) \\ \rho_1 u \\ \vdots \\ \rho_{N_s} u \\ E_{\text{ve}} u \end{pmatrix}, \quad \mathbf{G} = \begin{pmatrix} \rho v \\ \rho uv \\ \rho v^2 + p \\ \rho vw \\ v(E_t + p) \\ \rho_1 v \\ \vdots \\ \rho_{N_s} v \\ E_{\text{ve}} v \end{pmatrix}$$

$$\mathbf{H} = \begin{pmatrix} \rho w \\ \rho uw \\ \rho vw \\ \rho w^2 + p \\ w(E_t + p) \\ \rho_1 w \\ \vdots \\ \rho_{N_s} w \\ E_{\text{ve}} w \end{pmatrix}, \quad \mathbf{S} = \begin{pmatrix} 0 \\ 0 \\ 0 \\ 0 \\ 0 \\ \omega_1 \\ \vdots \\ \omega_{N_s} \\ \omega_{\text{ve}} \end{pmatrix} \tag{2}$$

III. Thermochemistry

A. Thermodynamic Models

The mixture total energy for a two-temperature gas model is expressed as

$$E_t(T,T_{\text{ve}}) = \sum_{i=1}^{N_s} \rho_i[(c_{v,i})_{\text{tr}} + (c_{v,i})_{\text{rot}}]T + \sum_{i=1}^{N_s} \rho_i h_{0,i} + E_{\text{ve}}(T_{\text{ve}}) + \frac{1}{2}\rho(u^2+v^2+w^2) \tag{3}$$

where $(c_{v,i})_{\text{tr}}$ and $(c_{v,i})_{\text{rot}}$ are the specific heats of fully excited translational and rotational modes, respectively. The vibrational–electronic energy for the two-temperature model can be evaluated from

$$E_{\text{ve}} = \sum_{i=1}^{N_s} E_{\text{ve},i} = \sum_{i=1}^{N_s} \rho_i e_{\text{ve},i} \tag{4}$$

$$e_{\text{ve},i}(T_{\text{ve}}) = e_i(T_{\text{ve}}) - ((c_{v,i})_{\text{tr}} + (c_{v,i})_{\text{rot}})T_{\text{ve}} - h_{0,i} \tag{5}$$

Here, the species internal energies $e_i(T_{\text{ve}})$ are calculated by a polynomial curve fit as a function of vibrational–electronic temperature from [8] for air species and [9] for Titan atmosphere.

In the thermal nonequilibrium model, the choice of a reaction temperature becomes somewhat ambiguous due to the presence of more than one temperature. The chemical reaction rates, in general, are functions of the collision frequency and of the Boltzmann factor, which gives the fraction of collisions above the activation energy. Although the collision frequency is only related to the translational temperature, it is known that highly vibrating molecules are more likely to dissociate. Therefore, Park [10] suggested to use a geometric average temperature for the calculation of the rates of the dissociating reactions:

$$T_d = \sqrt{TT_{\text{ve}}} \tag{6}$$

This reaction-temperature model is based on empirical results without any theoretical justification; however, this relation has been widely accepted within the scientific community.

Because both the total energy and vibrational–electronic energy are known after each iteration (they belong to the state vector), the translational–rotational temperature can be computed directly from Eq. (3). The vibrational–electronic temperature is calculated in two or three Newton iterations from Eqs. (4) and (5), starting from an initially guessed value.

B. Chemistry Model

Any elementary chemical reaction (identified with the index r) taking place in a gas flow is formally expressed as

$$\sum_{i=1}^{N_s} \nu'_{ir} X_i \rightleftharpoons \sum_{i=1}^{N_s} \nu''_{ir} X_i \tag{7}$$

where the species appearing on the left-hand side are reactants and those on the right-hand side are products, X_i denotes any given chemical species, and ν'_{ir} and ν''_{ir} are the stoichiometric coefficients for the ith reactant and product, respectively. An elementary reaction can proceed in both directions; when there is a perfect balance between forward and backward reaction, the process is in chemical equilibrium.

In accordance with the law of mass action, the net rate of production of species i by N_r elementary reactions is

$$\omega_{ir} = \text{MW}_i(\nu''_{ir} - \nu'_{ir})\left\{k_{f,r}\prod_{j=1}^{N_s}\left(\frac{\rho_j}{\text{MW}_j}\right)^{\nu'_{jr}} - k_{b,r}\prod_{j=1}^{N_s}\left(\frac{\rho_j}{\text{MW}_j}\right)^{\nu''_{jr}}\right\} \tag{8}$$

$$\omega_i = \sum_{r=1}^{N_r} \omega_{ir} \tag{9}$$

where ω_{ir} denotes the species source term due to the rth reaction, ω_i is the global species source term due to all the reactions included in the chemical model, $k_{f,r}$ is the forward reaction rate, and $k_{b,r}$ is the correspondent backward rate. The expression of ω_{ir} consists of a production term and a destruction term. Because this equation is also valid near equilibrium ($\omega_{ir} = 0$), the forward and backward reaction rates are related as

$$\frac{k_{f,r}}{k_{b,r}} = \prod_{j=1}^{Ns}\left(\frac{\rho_j}{\text{MW}_j}\right)^{\nu''_{jr}-\nu'_{jr}}_{\text{equilibrium}} = K_{c,r} \tag{10}$$

The equilibrium constant of the rth reaction $K_{c,r}$ for a perfect gas is a function of the temperature only:

$$\log K_{c,r}(T) = -\sum_{i=1}^{Ns}\frac{(\nu''_{ir}-\nu'_{ir})\hat{g}_i(T,p_0)}{\mathcal{R}T} - \log\left(\frac{\mathcal{R}T}{p_0}\right)\sum_{i=1}^{Ns}(\nu''_{ir}-\nu'_{ir}) \tag{11}$$

where $\hat{g}_i$ is the molar Gibbs free energy calculated with a polynomial curve fit from [8,9], and $p_0 = 1$ atm is the reference pressure. For the forward reaction coefficients, a semi-empirical formulation fitting experimental data, known as Arrhenius law, is used:

$$k_{f,r} = B_r T_d^{C_r} e^{-\frac{D_r}{T_d}} \tag{12}$$

The constants B_r, C_r, and D_r are available in the literature.

C. Vibrational Energy Source Term

The vibrational–electronic source term ω_{ve} in Eq. (2) is computed as

$$\omega_{\text{ve}} = \sum_{j=1}^{N_{\text{sp}}} \omega_{\text{ve},j} \tag{13}$$

$$\omega_{\text{ve},j} = \frac{E_{\text{ve},j}(T) - E_{\text{ve},j}(T_{\text{ve}})}{\tau_j} + \frac{\omega_j}{\rho_j}E_{\text{ve},j}(T_{\text{ve}}) \tag{14}$$

where the second term on the right-hand side in Eq. (14) is the rate of vibrational energy production due to the creation and destruction of polyatomic species by chemical reactions.

The vibrational relaxation time τ_j is calculated using the molar-averaged correlation developed by Millikan and White [11], which is based on the Laudau–Teller model [12,13]. The correlation is expressed as

$$\tau_j^{\text{MW}} = \frac{\sum_{i=1}^{N_{\text{sp}}} x_i \tau_{ij}}{\sum_{i=1}^{N_{\text{sp}}} x_i} \tag{15}$$

$$\tau_{ij} = \frac{\exp[A_{ij}(T^{-1/3} - 0.015\mu_{ij}^{1/4}) - 18.42]}{p/101,325} \tag{16}$$

$$A_{ij} = 1.16\times 10^{-3}\mu_{ij}^{1/2}\theta_j^{4/3} \tag{17}$$

$$\mu_{ij} = \frac{\text{MW}_i\text{MW}_j}{\text{MW}_i + \text{MW}_j} \tag{18}$$

For temperatures above 8000 K, Park's [14] high-temperature correction for the vibration relaxation time is adopted:

$$\tau_j^P = \sigma_j \bar{c}_j n_j \tag{19}$$

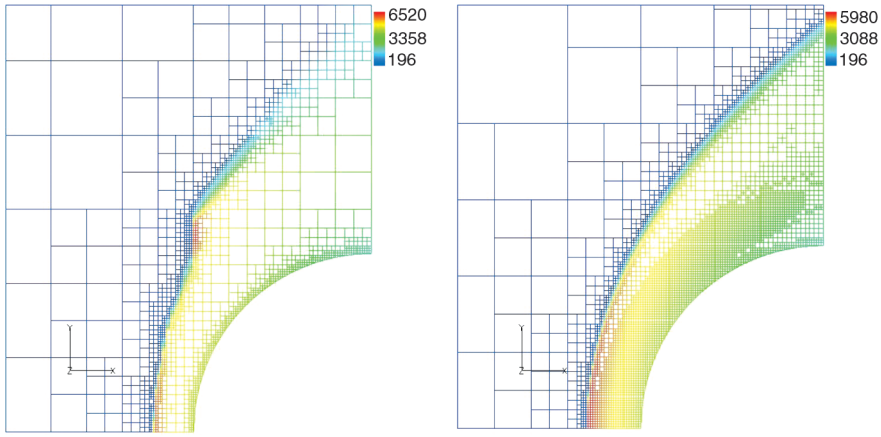

Fig. 1 Temperature contours of steplike shock formation during early stage of solution adaption (left) and enhanced solution with species gradient-based solution adaption (right).

where n_j is the number density of species j, $\bar{c}_j$ is the average molecular velocity, and σ_j is the effective cross section:

$$\bar{c}_j = \frac{8kT}{\pi \mathrm{MW}_j} \tag{20}$$

$$\sigma_j = 10^{21}\frac{50,000}{T^2} \tag{21}$$

The total vibrational relaxation time is

$$\tau_j = \tau_j^{\mathrm{MW}} + \tau_j^P \tag{22}$$

Park's [10] correction for high temperatures suggests that the vibrational relaxation process obeys a law somewhat similarly to the diffusion equation with respect to the vibrational energy level, rather than a linearly varying Landau–Teller model. According to Park, the relaxation time can be correlated with translational and vibrational temperatures at the upstream shock wave, where the relaxation process is initiated. Accordingly, the vibrational source term is modified to

$$\omega_{\mathrm{ve},j} = \frac{E_{\mathrm{ve},j}(T) - E_{\mathrm{ve},j}(T_{\mathrm{ve}})}{\tau_j}\left|\frac{T_{\mathrm{shock}} - T_{\mathrm{ve}}}{T_{\mathrm{shock}} - T_{\mathrm{ve,shock}}}\right|^{s-1} + \frac{\omega_j}{\rho_j}E_{\mathrm{ve},j}(T_{\mathrm{ve}}) \tag{23}$$

$$s = 3.5\exp(-5000/T_{\mathrm{shock}}) \tag{24}$$

In two- or three-dimensional flows, it is technically very difficult to trace the true value of the temperature immediately behind the shock for each streamline. It becomes even more difficult in unstructured-grid solvers. Therefore, T_{shock} and $T_{\mathrm{ve,shock}}$ are usually approximated with constant values representative of the flowfield. In the present work, these values are taken from the shock wave upstream of the stagnation point.

IV. Numerical Methods

A. AUSMPW+ Computational Scheme

Hypersonic flows are generally characterized by strong shock waves, leading to extremely large gradients in the flow properties. In these steep-gradient regions, even small nonphysical oscillations in the initial solution can lead to negative temperatures or pressures. During the initial stage of the present research, a minor oscillatory behavior was observed with Roe's approximate Riemann scheme in the regime in which the Mach number is higher than 15. To avoid such nonphysical oscillations, the AUSMPW+ scheme was chosen for the inviscid flux calculation. The detail formulation of this scheme is described in [15,16].

B. Point-Implicit Method

In the numerical solution of the species continuity equations, the vector of the chemical source terms $\boldsymbol{\omega} = (\omega_1, \ldots, \omega_{N_s})$ is treated in an implicit manner [17]. An explicit treatment leads to a time-step restriction due to stability limitations. The time step required for the stability of the chemical source terms can be orders of magnitude less than the time step necessary for the convective terms. Treating the source terms implicitly removes this limitation at the expense of a little computational effort. The set of species continuity equations applied to a flow cell of volume V in semidiscrete form is

$$\frac{\mathrm{d}\mathbf{q}}{\mathrm{d}t}V + \mathbf{R}_n = V\boldsymbol{\omega}_{n+1} \tag{25}$$

where $\mathbf{q} = (\rho_1, \ldots, \rho_{Ns})$ is the vector containing the species partial densities and the components of $\mathbf{R}$ are the species fluxes integrated over the cell surfaces. In Eq. (25) the convective terms are evaluated explicitly at t_n and the source terms are evaluated implicitly at t_{n+1}. The vector containing the source terms is linearized about the time level t_n as

$$\boldsymbol{\omega}_{n+1} \approx \boldsymbol{\omega}_n + \left(\frac{\partial\boldsymbol{\omega}}{\partial\mathbf{q}}\right)_n \frac{\mathrm{d}\mathbf{q}}{\mathrm{d}t}\Delta t \tag{26}$$

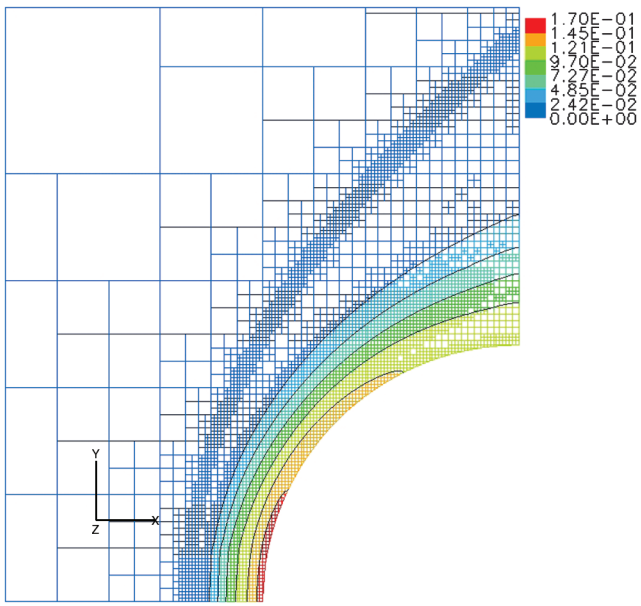

Fig. 2 Atomic oxygen molar fraction contours obtained with velocity divergence and species gradients based grid adaption (5-species air mixture).

Substituting this equation into Eq. (25) and rearranging yields

$$\frac{\mathrm{d}\mathbf{q}}{\mathrm{d}t} = \left[\mathbf{I} - \Delta t\left(\frac{\partial \boldsymbol{\omega}}{\partial \mathbf{q}}\right)_n\right]^{-1}\left(\boldsymbol{\omega}_n - \frac{\mathbf{R}_n}{V}\right) \tag{27}$$

Here, the right-hand side is evaluated entirely at the current time level and is fully explicit. This treatment requires to invert a matrix with dimension $N_s \times N_s$. The additional computational cost associated with the matrix inversion is largely compensated by avoiding the limitation on the explicit time step. The Jacobian matrix $\partial\boldsymbol{\omega}/\partial\mathbf{q}$ is evaluated analytically:

$$\frac{\partial \omega_i}{\partial \rho_k} = \frac{\mathrm{MW}_i}{\rho_k}\sum_{r=1}^{N_r}(\nu''_{ir} - \nu'_{ir})\left\{\nu'_{kr}k_{f,r}\prod_{j=1}^{N_s}\left(\frac{\rho_j}{\mathrm{MW}_j}\right)^{\nu'_{jr}} - \nu''_{kr}k_{b,r}\prod_{j=1}^{N_s}\left(\frac{\rho_j}{\mathrm{MW}_j}\right)^{\nu''_{jr}}\right\} \tag{28}$$

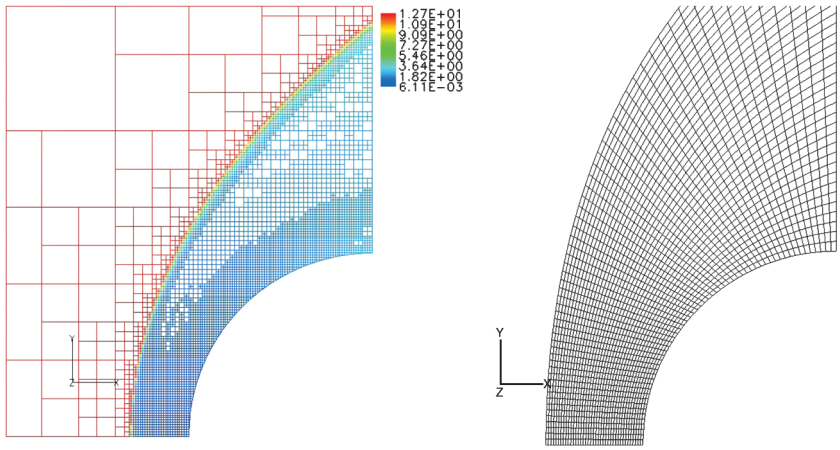

Fig. 3 Computational grid over the 0.5 m cylinder: NASCART-GT (left) and DPLR (right).

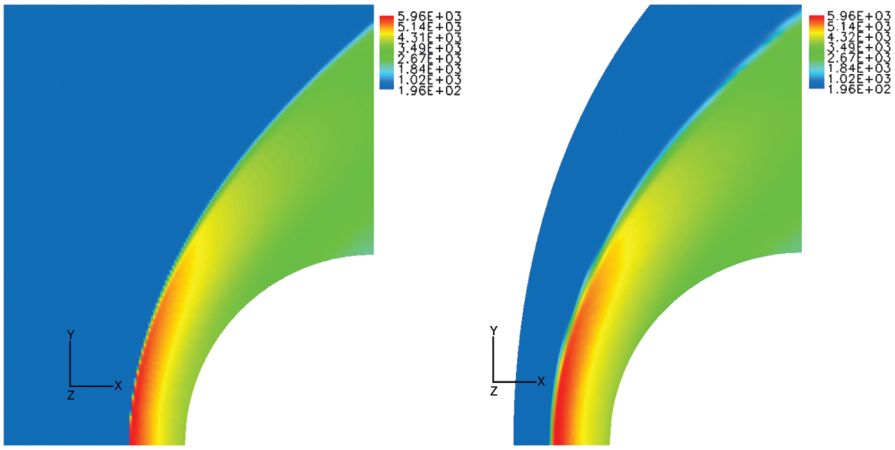

Fig. 4 Translational–rotational temperature: NASCART-GT (left) and DPLR (right).

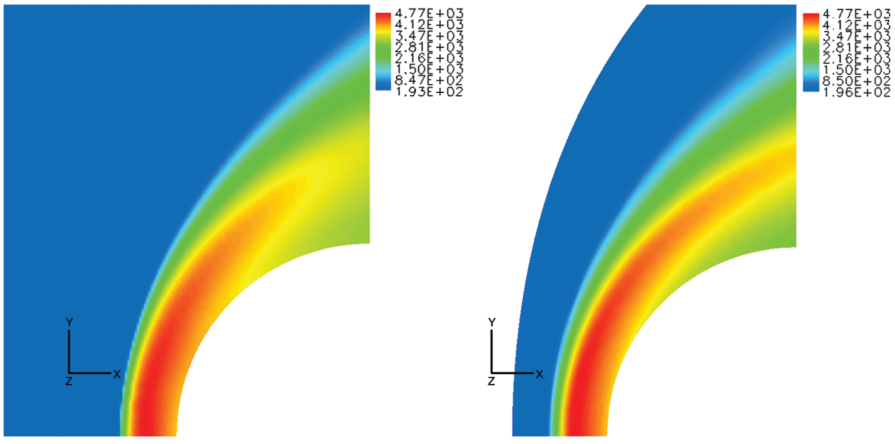

Fig. 5 Vibrational-electronic vs vibrational temperature: NASCART-GT (left) and DPLR (right).

The linear system (27), for its limited dimensions, is efficiently solved with a direct method such as the lower–upper decomposition.

C. Grid Refinement Based on Solution Adaption

The solution adaption methodology based on velocity divergence, discussed by Tu [7] and Marshall [18], provides adequate grid refinement along the shock waves and in rapid expansion regions, in which the velocity divergence is scaled by a characteristic length of the control volume to obtain a measure of the changing flow properties from one cell to another:

$$\tau_d = |\nabla \cdot \mathbf{v}| l^{3/2} \tag{29}$$

where l is the cube root of the cell volume and the power $3/2$ is to ensure that the adaption criteria's sensitivity diminishes with increasing refinement.

In this work, it was found that adaption to velocity divergence alone sometimes, but not always, caused stability problems for reacting-flow cases. The problems were caused during the early stages of solution adaption, when unrefined Cartesian cells induced steplike shock structures, as shown on the left in Fig. 1. Such

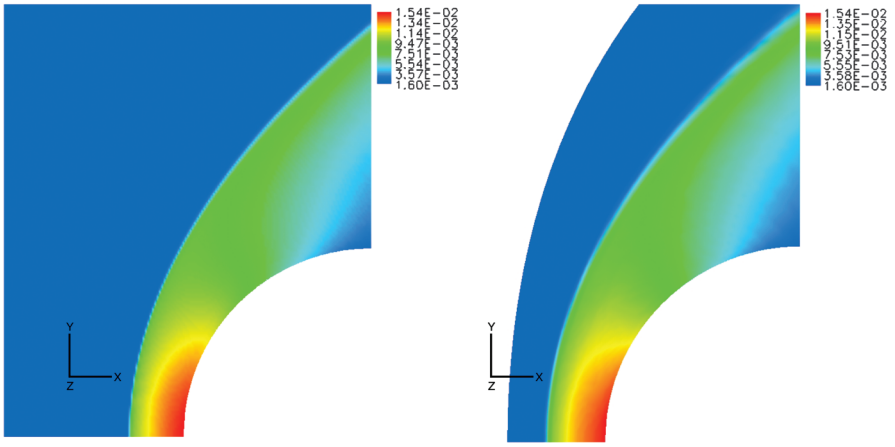

Fig. 6 Density: NASCART-GT (left) and DPLR (right).

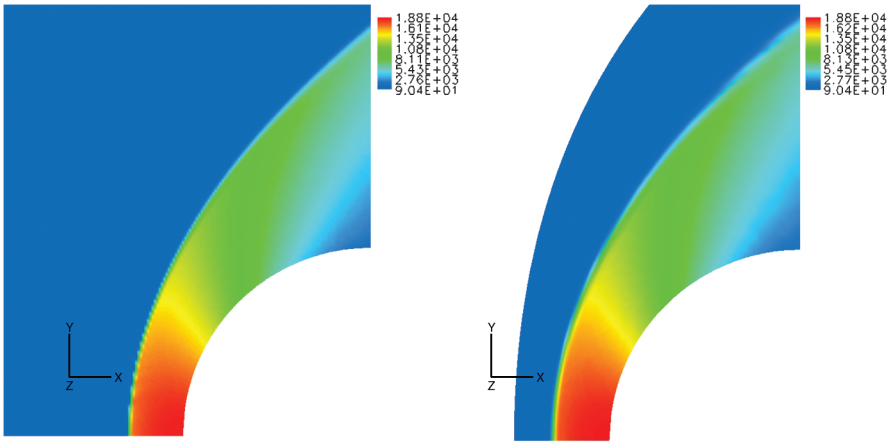

Fig. 7 Pressure: NASCART-GT (left) and DPLR (right).

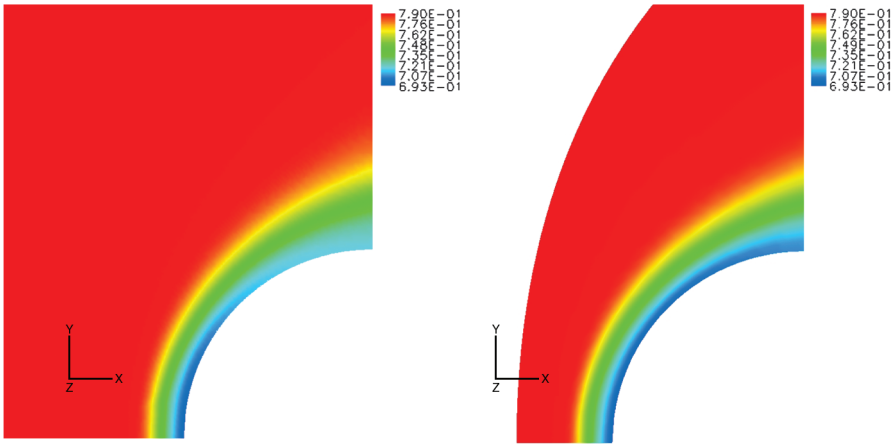

Fig. 8 N2 mass fraction: NASCART-GT (left) and DPLR (right).

nonphysical shock shapes could result in excessive dissociation of chemical species or create energy imbalances between surrounding cells. These kinds of problems during the intermediate calculations sometimes cause instabilities that could lead to solution divergence. Therefore, of present, the solution adaption methodology based on velocity divergence has been expanded to species concentration gradients, to avoid the instability problem and to increase the accuracy of solution in the downstream region of the shock, in which the finite rate chemical reactions happen. The validity of the numerical simulation of chemical nonequilibrium flows depends critically on species concentrations at a given state, which govern the energy transfer between chemistry and other internal energy modes. Therefore, resolving composition gradients along the flow streamline is necessary to obtain accurate flow solutions. The stable and accurate solution obtained from species-based solution adaption is shown on the right in Fig. 1. Figure 2 shows the evidence of grid

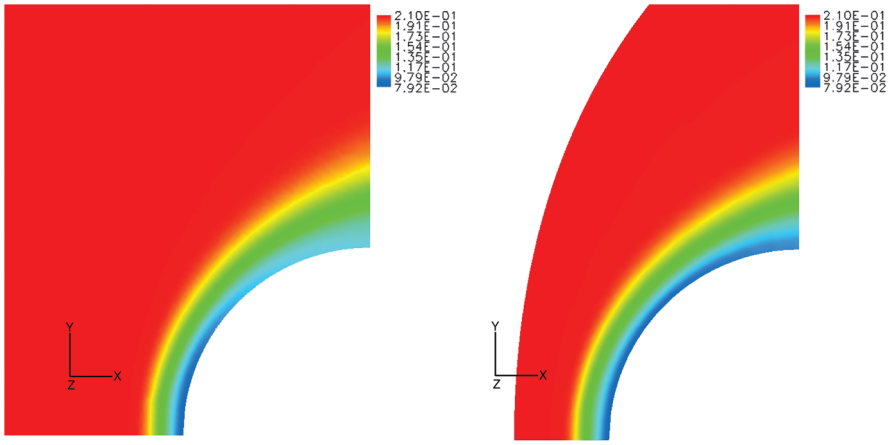

Fig. 9 O2 mass fraction: NASCART-GT (left) and DPLR (right).

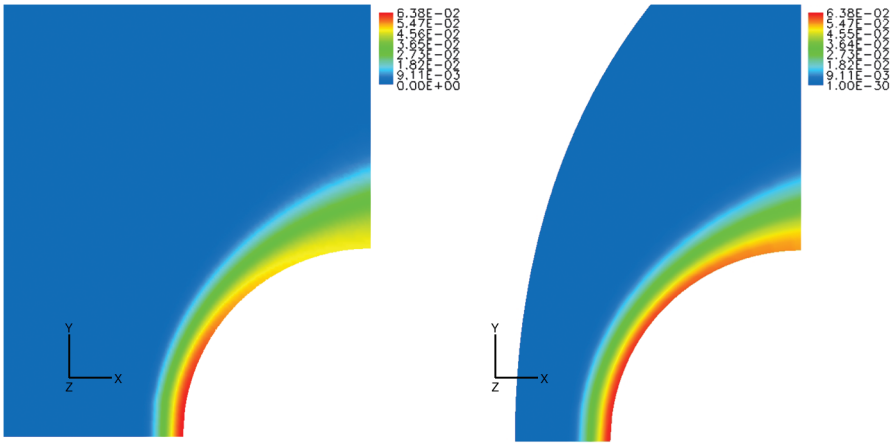

Fig. 10 NO mass fraction: NASCART-GT (left) and DPLR (right).

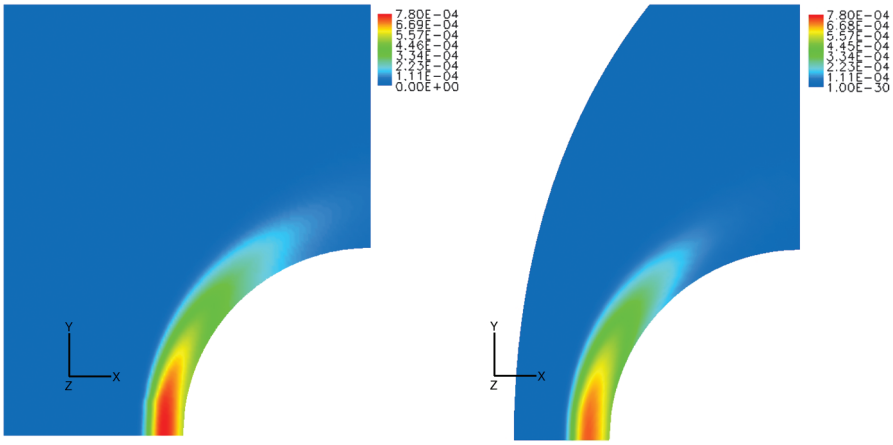

Fig. 11 N mass fraction: NASCART-GT (left) and DPLR (right).

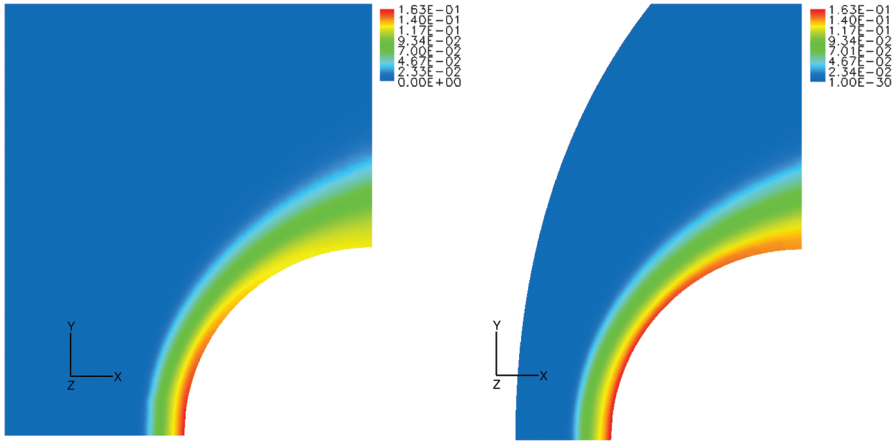

Fig. 12 O mass fraction: NASCART-GT (left) and DPLR (right).

adaption based on species gradient. The detailed description and verification for Figs. 1 and 2 are presented in the following Results section for the five-species air model case.

The formulation for the species gradient solution adaption is described as

$$\tau_c = N_s i \max_i^{N_s} |\nabla c_i| l^{3/2} \tag{30}$$

where c_i and N_s are the mass concentration of species i and the total number of species, respectively. The species gradient concentrations are computed from directly contacting neighbor cells using a second central-difference discretization.

The local species gradient τ_c is then compared with the root-mean-square value of the species gradient of the entire set of computational cells σ_c:

$$\sigma_c = \sqrt{\frac{1}{N}\sum_{n=1}^{N} \tau_c^2} \tag{31}$$

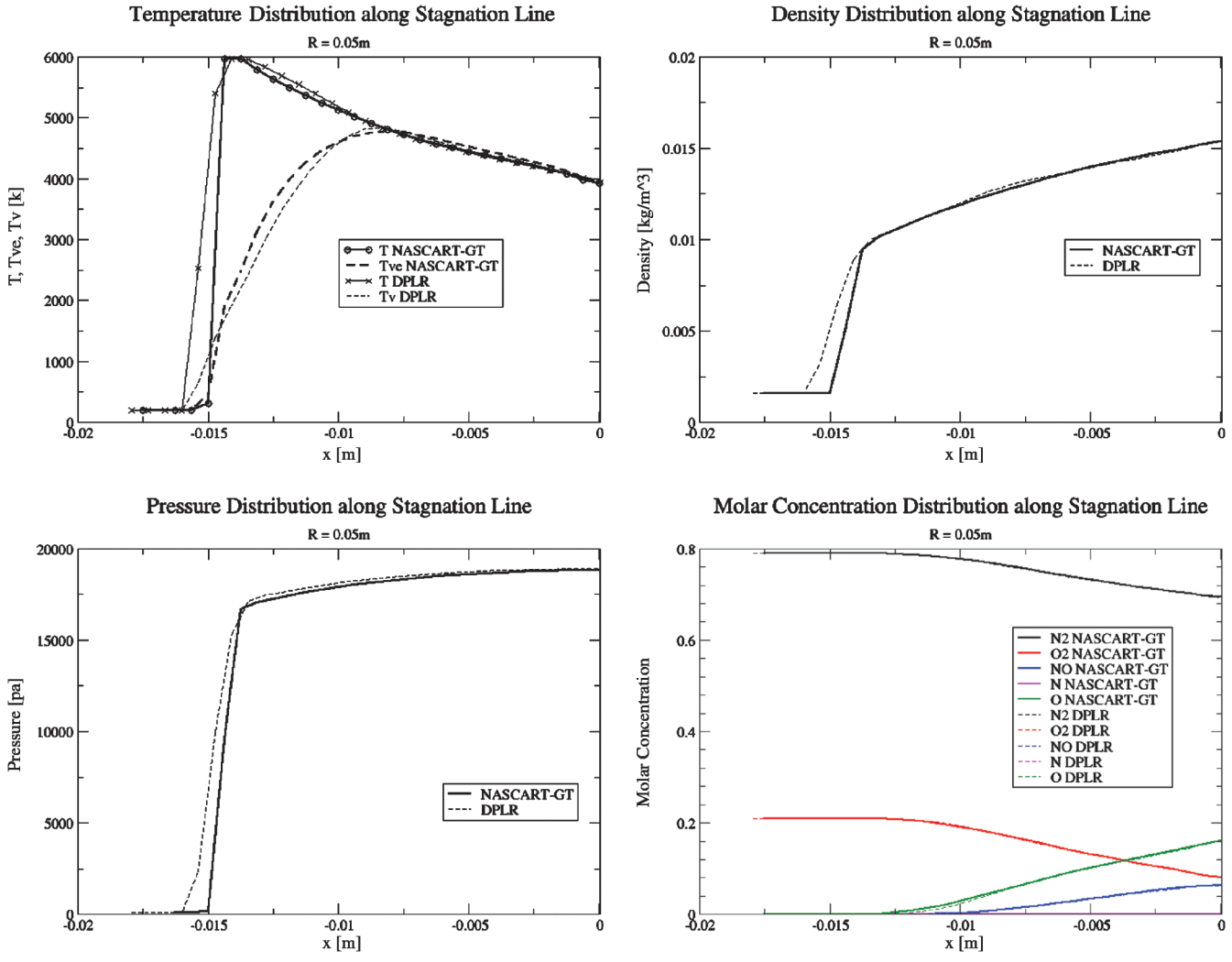

Fig. 13 Flow properties along the stagnation line: 5-species air mixture.

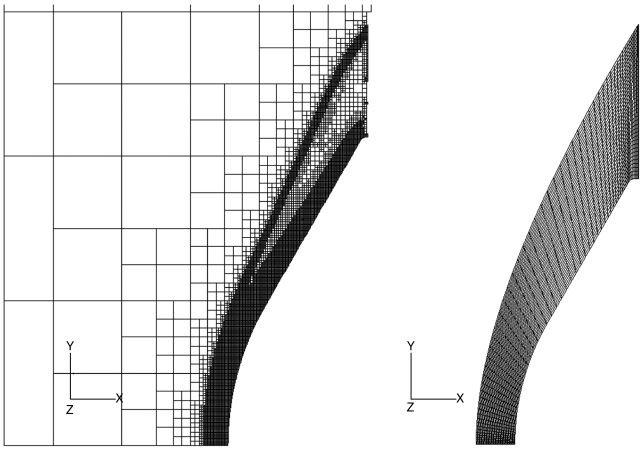

Fig. 14 Computational grid over Huygens probe: NASCART-GT (left) and DPLR (right).

where N is the total number of computational cells. Finally, cells are flagged for refinement and coarsening with adaption parameters $\alpha_{c,\min}$ and $\alpha_{c,\max}$. These adaption parameters are applied to every cell in the computational domain, excluding surface cells and outer boundary cells: refine if $\tau_c > \alpha_{c,\max}$, and coarsen if $\tau_c < \alpha_{c,\min}$.

Although the selection of the preceding parameters can be different for different cases, based on experience, $\alpha_{c,\min} = 0.1$ and $\alpha_{c,\max} = 1.0$ are typically sensitive enough to adapt most of the cells inside the shock layer, including cells near the stagnation region, and $\alpha_{c,\min} = 0.4$ and $\alpha_{c,\max} = 1.0$ are recommended to adapt the cells only near the stagnation region. Grid adaption is usually performed every 100 or 200 iterations for every cell in the computational domain, excluding surface cells and outer boundary cells. For the case described in Figs. 1 and 2, $\alpha_{c,\min} = 0.1$ and $\alpha_{c,\max} = 1.0$ are used at every 200 iterations.

V. Results

A. Five-Species Air Mixture

A test case consisting of a 2-D hypersonic flow around a circular cylinder ($R = 0.05$ m) is proposed to test the present thermochemical nonequilibrium solver. The freestream Mach number, pressure, and density are $M_\infty = 12.7$, $p_\infty = 90$ Pa, and $\rho_\infty = 0.0016$ kg/m^3, respectively. A total of 5 species with 17 chemical reactions have been considered. The forward reaction rates are from Park's 1993 model [19]. The total number of flow cells at the end of the computation was 7352 and the grid adaption was performed every 100 iterations based on velocity divergence and species gradients. Figure 3 (left) shows a good grid adaption along the shock wave and in the postshock region.

Figures 4–12 show the flow properties around the hypersonic cylinder. A steep rate of change of the chemical composition is present close to the wall, and few chemical reactions occur immediately downstream of the shock wave. This chemical nonequilibrium effects allow for a gradual density rise across the shock layers. On the other hand, the vibrational–electronic relaxation processes respond rapidly from the shock front and the vibrational–electronic mode becomes equilibrated with the translational mode, starting from the mid-shock-layer region.

To validate the new flow solver, a detailed comparison with an existing code has been performed. The reference solver is the NASA DPLR code. The left part of each figure presents the result of

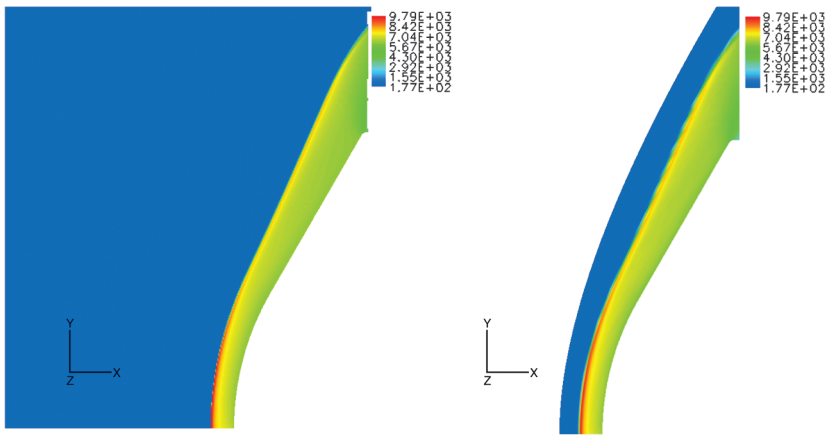

Fig. 15 Translational–rotational temperature: NASCART-GT (left) and DPLR (right).

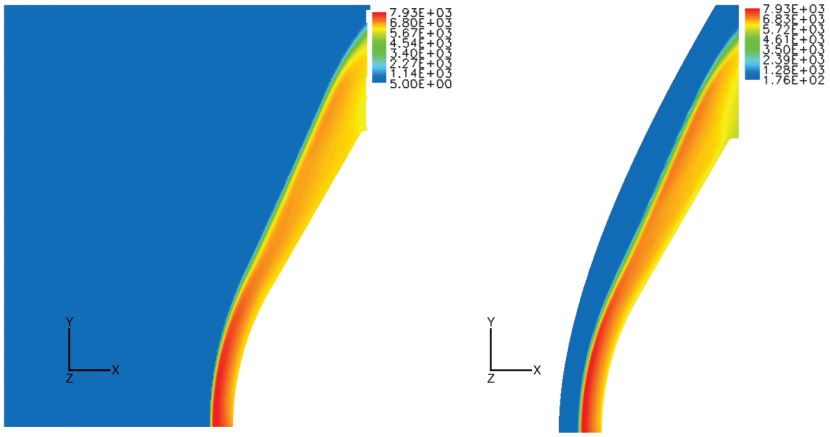

Fig. 16 Vibrational–electronic vs vibrational temperature: NASCART-GT (left) and DPLR (right).

NASCART-GT, and the right part shows the result of DPLR using a structured computational grid with 60×40 grid cells. Overall, the flow properties within the shock layer show a good agreement between NASCART-GT and with DPLR, although the recombination rates of the present work are a bit higher around the top surface of the cylinder, as shown in the Figs. 8 and 9.

This paper focuses in large part on a comparison of the ability to predict shock jump properties and thermochemical nonequilibrium processes. Thus, care was exercised to ensure that the cell spacing across the shock along the stagnation streamline was nearly the same for the NASCART-GT and DPLR results presented. This allows for a fairly direct comparison of shock property steepness along the stagnation streamline when the minimum shock normal grid spacing is the same for the two grid topologies. Because the cell spacing here was matched and because the Cartesian approach requires cell aspect ratios of nearly unity to model these geometries, the NASCART-GT grid had a total number of grid cells that was larger than that used for the structured-grid code.

Figure 13 summarizes the distribution of the flow properties along the stagnation line. The pressure curves show some underprediction

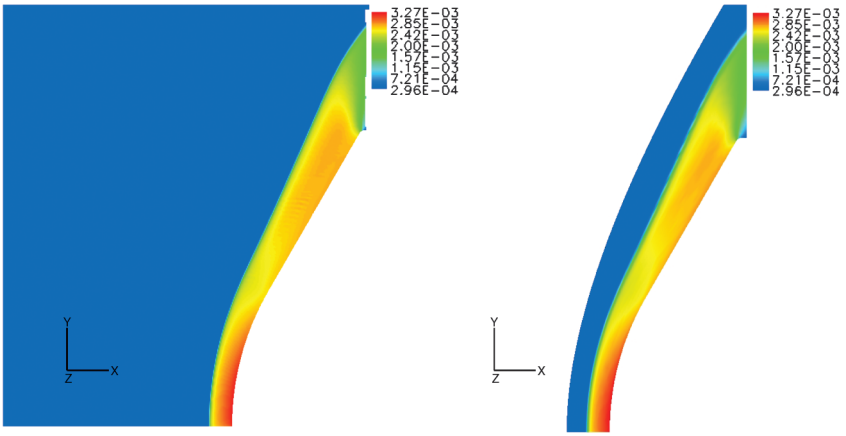

Fig. 17 Density: NASCART-GT (left) and DPLR (right).

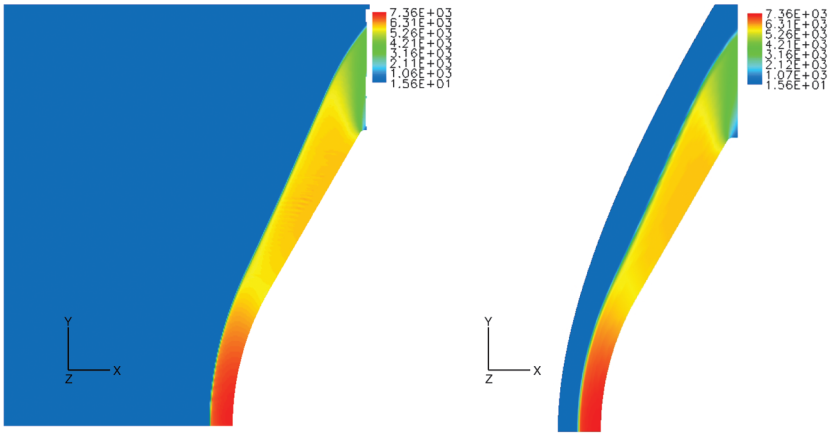

Fig. 18 Pressure: NASCART-GT (left) and DPLR (right).

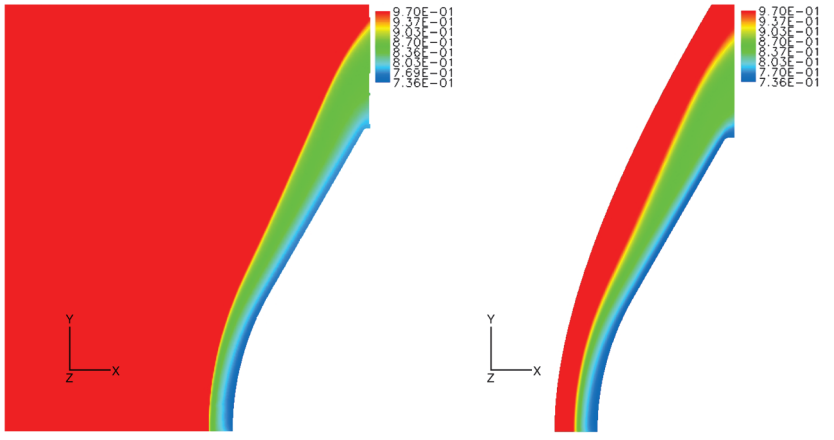

Fig. 19 N2 mass fraction: NASCART-GT (left) and DPLR (right).

at the shock front when compared with DPLR. The agreement becomes better closer to the surface and finally disagrees only 0.45% at the surface. The grid adaption capability of the present Cartesian method results in a sharper and better-resolved shock front. The vibrational–electronic temperature profiles show a slightly different relaxation slope. This discrepancy is expected because the present code uses a translational–rotational vs vibrational–electronic temperature system, and DPLR uses a translational–rotational–electronic vs vibrational temperature system. The difference between these two thermal models is also noted in a comparison between DPLR and LAURA in a recent publication [20]. The results of the two solvers regarding the chemical compositions along the stagnation line agree very well.

B. Thirteen-Species Titan Atmosphere Mixture

The peak dynamic pressure point of the Huygens probe during the Titan entry mission was simulated as second test case. This calculation was performed to validate the present thermochemical nonequilibrium solver under a N2-CH4-Ar mixture.

The Huygens probe [21] is a 60 deg half-angle sphere cone with a diameter of 2.7 m and a nose radius of 1.25 m. The freestream Mach

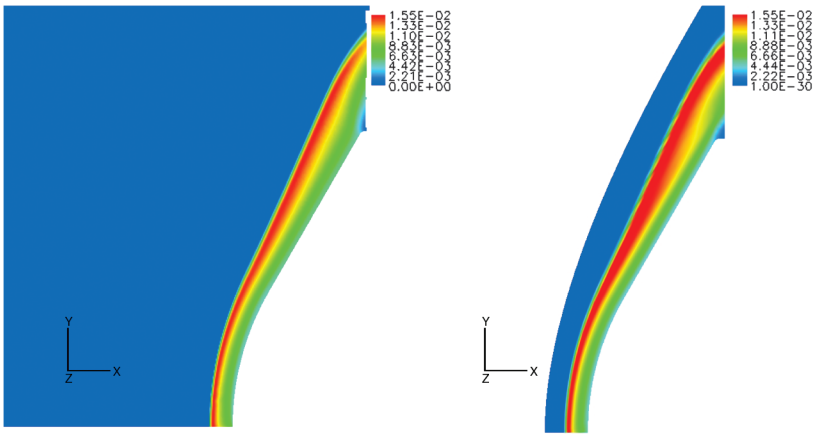

Fig. 20 CN mass fraction: NASCART-GT (left) and DPLR (right).

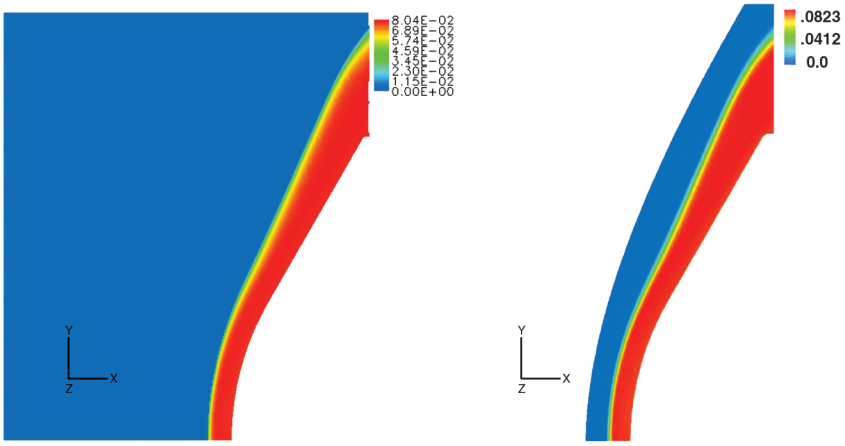

Fig. 21 H mass fraction: NASCART-GT (left) and DPLR (right).

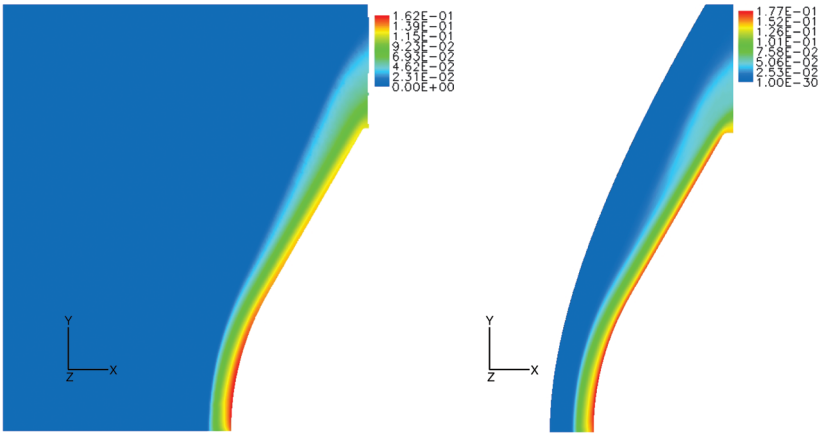

Fig. 22 N mass fraction: NASCART-GT (left) and DPLR (right).

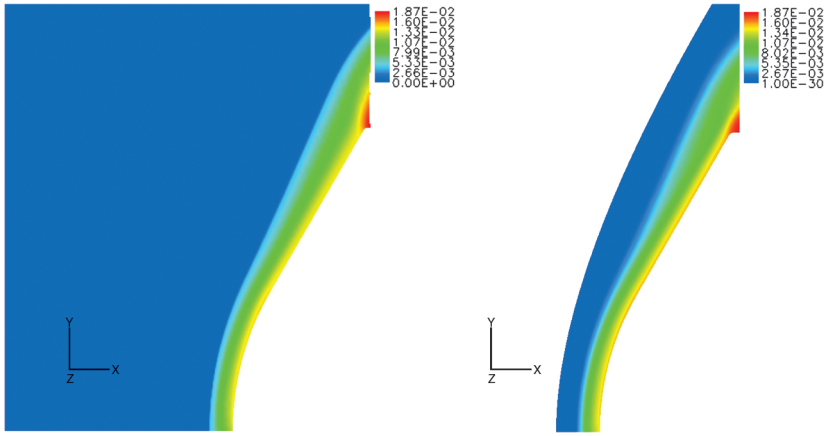

Fig. 23 C mass fraction: NASCART-GT (left) and DPLR (right).

number, angle of attack, pressure, and density are $M_\infty = 18.8585$, $\alpha = 0$, $p_\infty = 15.621$ Pa, and $\rho_\infty = 0.000296$ kg/m^3, respectively. A total of 13 species (N2, CH4, Ar, N, C, C2, CH, CH2, CH3, H, H2, CN, and NH) with 24 chemical reactions are used. The forward reaction rates are taken from Gökçen [22]. The total number of flow cells at the end of the simulation is 11,224 with 512 surface cells in the radial direction. Solution adaption was performed every 100 iterations, based on velocity divergence and species gradients.

The solution of this axisymmetric test case was also compared with DPLR. Figure 14 shows the NASCART-GT grid and the structured grid of DPLR with 60×40 cells. Again, the cell spacing across the shock along the stagnation streamline was nearly the same for the NASCART-GT and DPLR results presented. The left section in each figure, from 15–23, is the result of the present work; the right section is the result of DPLR. Despite the complexity of the chemical systems, the value and distribution of flow properties match well overall with the validation code, except for some minor discrepancies. The temperature contours agree reasonably well, with only a 2% difference at the stagnation point. Our solution has a better-resolved shock wave, as discussed in the earlier cylinder case. For the density contours, it is interesting to note that both solvers predict the location of the highest density point at about +0.07 m from the

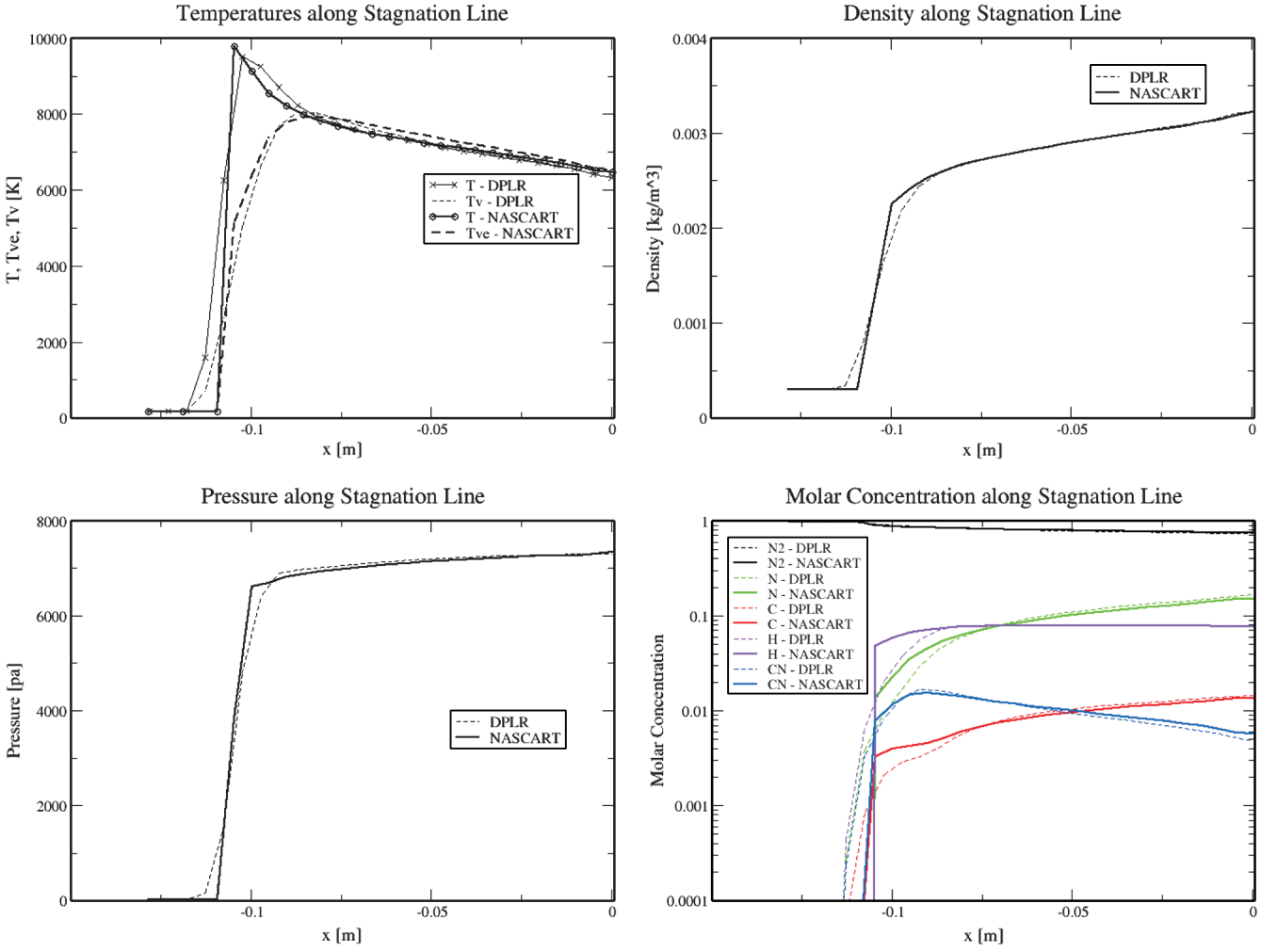

Fig. 24 Flow properties along the stagnation line, 13-species Titan atmosphere mixture.

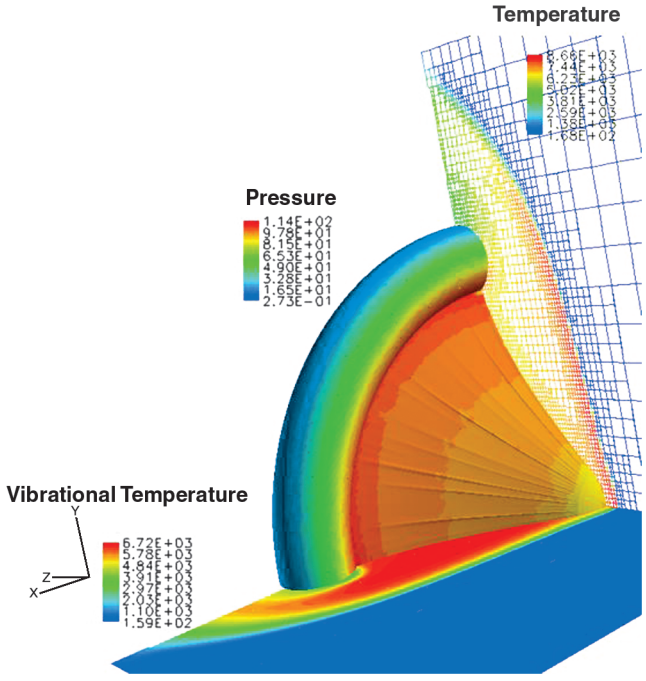

Fig. 25 Unstructured Cartesian grid over a 3-D clamped ballute: translational–rotational temperature (*X* plane), vibrational–electronic temperature (*Y* plane) and pressure (surface).

stagnation point in the radial direction. The density value at this point is about 2% less than that of DPLR. Also, the density and the pressure are slightly higher in the shock layer near the midspan. In terms of chemical composition, DPLR solution is a bit more reactive than NASCART-GT solution, but the distribution of species show similar patterns.

Figure 24 shows the flow properties along the stagnation line. They also agree well with the reference code, except for a more discrete shock front computed by NASCART-GT.

C. Three-Dimensional Ballute Analysis

Simulations of a clamped ballute were performed to demonstrate the 3-D capability of the current solver. A total of 187,043 cells were used with solution adaption based on velocity divergence and species gradients performed every 100 iterations. The same gas mixture of the previous test case is considered. Only one-quarter of the windward side of the ballute was simulated to avoid numerical challenges in computing the dead zone on the leeward side. The 3-D Cartesian grid, the pressure, and the translational and vibrational temperature profiles are shown in Fig. 25. The detailed flow analysis of this case is described in [23] along with details of the structural deformation of the flexible ballute.

VI. Conclusions

A solution-adaptive unstructured Cartesian grid solver for nonequilibrium flows was developed starting from a perfect gas solver, NASCART-GT. This new code was developed by implementing a set of species continuity equations and thermodynamic routines to handle a mixture of thermally perfect gases. Then a vibrational nonequilibrium model was added to compute two-temperature flows. The accuracy of this work was verified against DPLR (NASA Ames Research Center's structured-grid nonequilibrium solver). In general, the results of the improved NASCART-GT agrees well with the reference code. As expected, the AUSMPW+ scheme with MUSCL data reconstruction effectively resolves the large gradients of the flow properties at the shock wave. The point-implicit technique used for the source terms allows the original Courant–Friedrichs–Lewy constraints of the explicit solver to be maintained. Favorable comparison of the present results with a highly regarded structured-grid solver provides confidence in the present approach and suggests that it is suitable for continued research and development. This work represents a first step toward the accurate investigation of the aerodynamics of deformable hypersonic entry vehicles presented in [23]. A future recommendation would be to expand the present flow solver to treat hypersonic viscous flows and radiation effects with the aim to quantify convective and radiative heat transfer.

References

[1] Aftosmis, M. J., and Baron, J. R., "Adaptive Grid Embedding in Nonequilibrium Hypersonic Flow," AIAA Paper 89-1652, June 1989.

[2] Gnoffo, P. A., "Computational Fluid Dynamics Technology for Hypersonic Applications," AIAA Paper 2003-3259, July 2003.

[3] Gnoffo, P. A., and White, J. A., "Computational Aerothermodynamic Simulation Issues on Unstructured Grids," AIAA Paper 2004-2371, June 2004.

[4] Mavriplis, D. J., "Revisiting the Least-Squares Procedure for Gradient Reconstruction on Unstructured Meshes," NASA, Technical Report CR-2003-212683, 2003.

[5] Nompelis, I., Drayna, T. W., and Candler, G. V., "Development of a Hybrid Unstructured Implicit Solver for the Simulation of Reacting Flows over Complex Geometries," AIAA Paper 2004-2227, June 2004.

[6] Nompelis, I., Drayna, T. W., and Candler, G. V., "A Parallel Unstructured Implicit Solver for Hypersonic Reacting Flow Simulation," AIAA Paper 2005-4867, June 2005.

[7] Tu, S., "Development of A Solution Adaptive Cartesian-Grid Solver for 2-D Thermochemical Nonequilibrium Flows," Ph.D. Thesis, Georgia Inst. of Technology, Atlanta, 2001.

[8] Gupta, R. N., Yos, J. M., Thompson, R. A., and Lee, K. P., "A Review of Reaction Rates and Thermodynamic and Transport Properties for an 11-Species Air Model for Chemical and Thermal Nonequilibrium Calculation to 30,000 K," NASA, Reference Publication 1232, 1990.

[9] McBride, B. J., Zehe, M. J., and Gordon, S., "NASA Glenn Coefficients for Calculating Thermodynamics Properties of Individual Species," NASA, TP-2002-211556, Sept. 2002.

[10] Park, C., "Assessment of Two-Temperature Kinetic Model for Ionizing Air," AIAA Paper 87-1574, 1987.

[11] Millikan, R. C., and White, D. R., "Systematics of Vibrational Relaxation," *Journal of Chemical Physics*, Vol. 39, No. 12, 1963, pp. 3209–3213. doi:10.1063/1.1734182

[12] Landau, L., and Teller, E., "Zur Theorie der Schalldispersion," *Physikalische Zeitschrift der Sowjetunion*, Vol. 10, No. 1, 1936, p. 34.

[13] Vincenti, W. G., and Kruger, C. H. Jr., *Introduction to Physical Gas Dynamics*, Krieger, Malabar, FL, 1967.

[14] Park, C., "Problems of Rate Chemistry in the Flight Regimes of Aeroassisted Orbital Transfer Vehicle," *Progress in Astronautics and Aeronautics*, Vol. 96, AIAA, New York, 1985.

[15] Kim, K. H., Kim, C., and Rho, O. H., "Accurate Computations of Hypersonic Flows Using AUSMPW+ Scheme and Shock-Aligned Grid Technique," *Journal of Computational Physics*, Vol. 174, No. 1, 2001, pp. 38–80. doi:10.1006/jcph.2001.6873

[16] Kim, K. H., Kim, C., and Rho, O. H., "Methods for the Accurate Computations of Hypersonic Flows," AIAA Paper 98-2442, 1998.

[17] Sheer, S., Martinelli, L., and Jameson, A., "Simulation of Supersonic Reacting Hydrocarbon Flows With Detailed Chemistry," AIAA Paper 1997-3240, 1997.

[18] Marshall, D. D., "Extending the Functionalities of Cartesian Grid Solvers: Viscous Effects Modeling and MPI Parallelization," Ph.D. Thesis, Georgia Inst. of Technology, Atlanta, 2002.

[19] Park, C., "Review of Chemical-Kinetic Problems of Future NASA Missions, 1: Earth Entries," *Journal of Thermophysics and Heat Transfer*, Vol. 7, No. 3, 1993, pp. 385–398. doi:10.2514/3.431

[20] Hash, D., Olejniczak, J., Wright, M., Dinish, P., Pulsonetti, M., Hollis, B., Gnoo, P., Barnhard, M., Nompelis, I., and Candler, G., "FIRE II Calculations for Hypersonic Nonequilibrium Aerothermodynamics Code Verification: DPLR, LAURA, and US3-D," AIAA Paper 2007-605, 2007.

[21] Wright, M. J., Hollis, B. R., and Bose, D. W., "Post-Flight Aerothermal Analysis of Huygens Probe," ESA Paper WPP-263, 2005.

[22] Gökçen, "N2-CH4-Ar Chemical Kinetic Model for Simulations of Atmospheric Entry to Titan," AIAA Paper 2004-2469, 2004.

[23] Lee, J. W., Rohrschneider, R. R., Run, S. M., and Braun, R. D., "Flow-Structure Analysis of a Clamped Ballute in Titan's Atmosphere," AIAA Paper 2007-4308, June 2007.